Research article

Exploring the CO_2 photocatalytic evolution onto the CuO (1 1 0) surface: A combined theoretical and experimental study

O. Castro-Ocampo [a,*], J.C. Ochoa-Jaimes [a], Christian A. Celaya [b],
J. González-Torres [c], L. González-Reyes [c], I. Hernández-Pérez [c], V. Garibay-Febles [d],
Oscar A. Jaramillo Quintero [a], Jesús Muñiz [a], R. Suárez-Parra [a]

[a] Instituto de Energías Renovables, Universidad Nacional Autónoma de México, Priv. Xochicalco s/n, Col. Centro, Temixco, Morelos, CP 62580, Mexico
[b] Centro de Nanociencias y Nanotecnología, Universidad Nacional Autónoma de México, Km 107 Carretera Tijuana-Ensenada, Ensenada, B.C., C.P. 22800, Mexico
[c] Universidad Autónoma Metropolitana-A, Departamento de Ciencias Básicas, Av. Sn. Pablo Xalpa No. 180, San Martin Xochinahuac, Azcapotzalco, 02128, CDMX, 02200, Mexico
[d] Instituto Mexicano del Petróleo, Eje Central Lázaro Cárdenas Norte 152 Col. San Bartolo Atepehuacan, CDMX, C.P 07730, Mexico

ARTICLE INFO

ABSTRACT

A combined theoretical and experimental study was performed to elucidate the photocatalytic potential of tenorite, CuO (1 1 0) and to assess the evolution pathway of carbon dioxide (CO_2) evolution pathway. The calculations were performed with density functional theory (DFT) at a DFT + U + J0 and spin polarized level. The CuO was experimentally synthesized and characterized with structural and optical methodologies. The band structure and density of states revealed the rise of band gaps at 1.24 and 1.03 eV with direct and indirect band gap nature, respectively. These values are in accordance with the experimental evidence at 1.28 and 0.96 eV; respectively, which were obtained by UV-Vis DRS. Such a behavior could be related to enhanced photocatalytic activity among copper oxide materials. Experimental evidence such as SEM images and work function measurements were also performed to evaluate the oxide. The redox potential suggests a catalytic character of tenorite (1 1 0) for the CO_2 transformation through aldehydes (methanal) intermediate formation. Furthermore, a route through methylene glycol $CH_2(OH)_2$ was also explored with the theoretical methodology. The reaction path exhibits an immediate reduction of H_2O_2 into a $^{\bullet}OH$ radical and an $[OH]^-$ anion, in the first step. This $^{\bullet}OH$ radical attacks a double bond (C = O) of CO_2 to form bicarbonate ($[HCO_3]^-$) and subsequently, carbonic acid (H_2CO_3). The carbonic acid reacts with other $^{\bullet}OH$ radical to finally form orthocarbonic acid ($C(OH)_4$).

1. Introduction

The effects of global warming are evident on a general scale. As a consequence, the meteorological phenomena such as El Niño and La Niña occur at a larger extent [1], as is widely known [2]. CO_2 accumulation is responsible to boost these effects, the

overproduction of this gas is mainly due to human activity. Therefore, reducing the high concentration of CO_2 into the atmosphere represents a challenge that the scientific community is aimed to face [3,4]. In this regard, photocatalyst materials are very attractive to overcome this issue, and one of the most promising semiconductors to be used in the CO_2 photoreduction process [5–8].

Recently, the photocatalytic CO_2 reduction using nanostructured semiconductors has become essential to remove pollutants, in this process the chemical reactions are activated by solar energy. The semiconductor materials are required to allow electron transfer from the valence band (VB) to the conduction band (CB), favoring the formation of charge carriers (e^- /h^+) at the semiconductor surface. This process enables the CO_2 reduction towards added-value products, such as methanol (CH_3OH), methane (CH_4), formic acid (HCOOH), formaldehyde (HCHO) and carbonic acid (H_2CO_3) [9]. In recent years, different nanostructured semiconductors have been proposed to improve the efficiency of current CO_2 photo-reduction processes [9–16]. The role played by the catalyst surface in the CO_2 evolution process has been elucidated by computational modeling [17]. Despite a large number of works aimed on the CO_2 photoreduction, the design of the synthesis to enhance the adsorption ability is still in debate, since the understanding of the recombination rate of the charge carriers and the photocatalytic performance in the novel photocatalysts represent a current challenge.

Cuprous-based semiconductors are low-cost materials with a suitable range of band gap energies and favorable band alignment for the CO_2 reduction reaction [18]. Copper oxide (CuO) is considered an important *p*-type semiconductor with a band gap ranging from 1.2 to 1.9 eV, which also shows efficient light absorption [18]. Recently, Guo et al. [19] performed the synthesis of Sn catalysts, dispersed on a defective CuO_2 support in order to enhance the CO_2 electroreduction to methanol. They obtained a high methanol Faradaic efficiency of 88.6% with a current density of 67.0 mAcm^{-2}. Jia et al. [20] synthesized a sulfur-doped spherical coral-like CuO (S-CuO) catalyst. They reported a Faradaic efficiency of 48.4%, in the electrochemical CO_2 reduction to ethylene. DFT calculations show the direct participation of the S atom in CO_2 activation [20]. It is worth mentioning that the catalytic potential of tenorite has been theoretically studied in previous works for different applications to those of CO_2 transformation. That is Kasai et al. [21] investigated the CuO (1 1 0) surface in the NO adsorption and dissociation process via spin-polarized DFT calculations. They found an energy barrier of 1.08 eV in the NO adsorption process, which is close to that obtained with the CuO_2 (111) surface [21]. Jiang et al. [22] incorporated CuO into the structure of graphitic carbon nitride (g-C_3N_4) structure to enhance the CO_2 reduction to methanol via photoelectrocatalytic reaction. They found that the CuO/g-C_3N_4 heterostructured photocatalyst exhibits a Faradaic and a quantum efficiency of 75.0% and 8.9%, respectively. In this context, the use of CuO nanostructure has been widely studied in photoelectrocatalysis applications. However, a deeper understanding from an atomistic point of view is still required on the role that the CuO surface plays in the chemical transformations.

It is essential to realize that, to control a photocatalytic process, two factors are required: the adsorption of the molecules involved in the process and the absorption of light radiation by the semiconductor. The interplay of these two factors leads to charge carrier generation, and with the semiconductor redox potential, the enhancement of the oxidation or reduction of the adsorbed molecules. Tenorite CuO has been studied mainly in heterojunctions due to its low band gap and, consequently, selective photocatalytic potential [23,24]. Nevertheless, CuO has not been studied in photocatalytic processes for CO_2 reduction/transformation. The aim of this work is to evaluate the photocatalytic potential of the CuO (1 1 0) to transform CO_2 into carbon compounds of added value, using first-principles calculations. The validity of the tenorite modeling is also assessed with X-ray diffraction (XRD), work function and optical gap experimental evidence. Scanning electron microscopy (SEM) characterization is also presented to show the morphology of cuprite oxide.

In the present study, the transformation of the reaction pathway of CO_2 in the presence of the tenorite (CuO) surface is more likely to follow than other Cu-based surfaces that consider formic acid, aldehyde, carbon monoxide as intermediates, due to the narrow band gap and redox potential values present in tenorite. The CuO photocatalytic potential was evaluated with DFT+U+J calculations and the reaction path was also modeled with the transformation of CO_2 into H_2CO_3, C(OH)$_4$, by $^{\bullet}$OH addition reactions for the CO_2 activation. The products $CH_2(OH)_2$, CH_3OH, and CH_4 were subsequently found by reduction reactions in theoretical calculations.

2. Experimental and theoretical methodologies

2.1. Experimental section

Copper oxide synthesis: Copper oxide nanoparticles were initially prepared in a solution of cupric chloride ($CuCl_2 \bullet 2H_2O$, Fermont). Subsequently, a solution of sodium hydroxide (NaOH, Fermont) was added for a molar ratio of 1:2. This mixture was stirred on a magnetic plate for 30 minutes at 600 rpm. When this time elapsed, the solution was filtered in a filter paper. As the last step, the final paste was subjected to a heat treatment at 500 °C for 2hr.

Structural characterization: X-ray diffraction (XRD) pattern of CuO was measured on a Rigaku DMAX2200 difractometer using an X-ray radiation source of Cu Kα at a wavelength of 1.54 nm. The diffractograms were measured at a given interval of $5° \leq 2\theta \leq 80°$.

Optical measurements were performed by means of UV-Vis DRS (Diffuse Reflectance Spectrophotometry) on a UV-310PC spectrophotometer (Shimadzu), equipped with an integration sphere (coated with a $BaSO_4$ as reference), operating in diffuse reflectance mode (from 200 nm to 900 nm). To determine the experimental band gap (E_g), the Kubelka-Munk equation was used.

To measure the work function value of the sample, the powder was dispersed in deionized water using an ultrasonic bath. Then, 80 μL of the dispersion was deposited onto fluorine-doped tin oxide substrate by spin coating technique and heated in an electric oven. The work function value was obtained by Kelvin probe system (KP Technology SKP5050) with a gold tip under dark conditions.
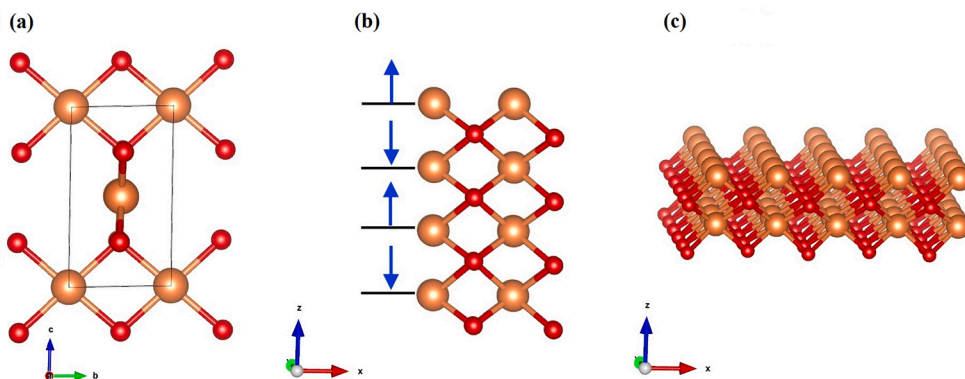
Fig. 1. (a) Tenorite primitive cell, (b) Tenorite (1 1 0) surface unit cell with vacuum (blue arrows represent spin values), (c) Surface super-cell with vacuum in the z direction.

2.2. Computational details

All calculations were performed using DFT [25] as implemented in the Quantum ESPRESSO code [26]. The generalized gradient approximation (GGA) at the Perdew-Burke-Ernzerhof (PBE) exchange-correlation level [27] with a Hubbard (**U** + **J0**) correction [28,29] was used for such computations, with the spin-polarization level. The work function calculations and the electronic structure properties were analyzed with a non-relativistic approach. The calculations were performed with the following convergence criteria: 1×10^{-6} Ry for the convergence threshold in the SCF scheme and 1×10^{-5} Ry for the initial threshold in the iterative diagonalization procedure (eigenvalue convergence). The kinetic energy cut-off for wavefunctions was set to 40 Ry (544 eV). The Monkhorst and Pack grid [30] was set to a $4 \times 4 \times 4$ k-points grid for the Brillouin zone in the primitive cell of tenorite (see Fig. 1 (a)). This configuration was used for the density of states (DOS) and for the calculation of the band structure by following the path Γ - $C|C2$ -$Y2$-Γ-$M2$-$D|D2$-A-$\Gamma|L2$-Γ-$V2$-K path. It is worth mentioning that despite other theoretical works on tenorite have been reported before, this particular k-path has not been explored. In addition, a $3 \times 3 \times 1$ k-grid was set for the unit cells that were used for the computations of work function and the search of the minimum energy path (MEP) (Fig. 1 (b) and (c), respectively) in the string computations, which is described below.

The search for MEPs [31,32] was performed with the Fritz Haber Institute *ab initio* molecular simulations (FHI-aims) computational code [33–35]. In this case, the GGA-PBE level was also used [27] and the set of numerical basis set *tier*1 was implemented for all atoms [34]. London interactions of van der Waals (vdW) type were modeled with the Tkatchenko-Scheffler correction [36]. The criteria for the energy convergence, electron density, and forces in optimization cycles were set to 1×10^{-4} eV, 10^{-5} electrons, and 0.01 eVÅ^{-1}, respectively. Moreover, the zeroth-order relativistic approximation (ZORA) [37] was also applied in the calculations due to the possible significant scalar relativistic effects that play a role in the description of the electronic structure of the metal oxides under study. A Monkhorst-Pack [30] grid with $3 \times 3 \times 1$ k-points was implemented to sample the Brillouin zone. All criteria were used to model the reactions of interest on the catalyst surface of the tenorite at the (1 1 0) facet, which was previously optimized (see Fig. 1 (b)) with cell parameters a = 12.9 Å, b = 13 Å, and c = 30 Å (a vacuum is given in the z direction to ensure that there will be no spurious interactions with the images of the unit cells, which are produced from the definition of periodic conditions). The angle values in the unit cell are α = 90°, β = 90° and γ = 87.497°. Furthermore, to locate the appropriate transition states (TS), the climbing image (CI) [38] version of the improved string method was performed to identify the saddle points. In this approach, an equidistant spacing is considered during all interactions for each image along the entire path. The DFT/PBE + vdW methodology [36] was used to include the intermolecular attractions among the slab models and the species on the surface. The reaction pathways were obtained with a convergence threshold of 0.5 eV for the string and CI-string methods [38]. The path was evaluated in 16 images (steps), initializing with a geometrical disposition of the reactants, and ending up with the products in each of the pathways under study. The details of this analysis are presented in section **S2** of the supplementary information (SI).

The adsorption energy (E_{M1ads}) was calculated according to the following equation:

$$E_{M1ads} = E_{tot} - E_{M|surf} - E_{M1|M} + E_M. \tag{1}$$

The interaction energy between $M1$ with M, and M with CuO (1 1 0) surface is expressed as $E_{M1|M}$ and $E_{M|surf}$, respectively. In that equation, $E_{M1|M}$ and $E_{M|surf}$ were calculated by using SCF calculations for the $E_{M1|M}$ and $E_{M|surf}$ in the same position that they occupy within the unit cell of the full system. Moreover, M represents the molecules adsorbed onto the CuO (1 1 0) surface in the same position that they would occupy within the unit cell of the complete system.

Note that in Eq. (1), the energy of the remaining molecules (M) is subtracted twice (in the $E_{M|surf}$ term and in the $E_{M1|M}$ term). Therefore, the energy of the isolated M molecule is added back.

In this respect, Eq. (1), considers that the negative E_{M1ads} values that are larger than 0.5 eV correspond to an enhanced adsorption mechanism that can be interpreted as chemisorption, and E_{M1ads} values that are smaller than 0.5 eV represent cases of weak adsorption, or physisorption [39].
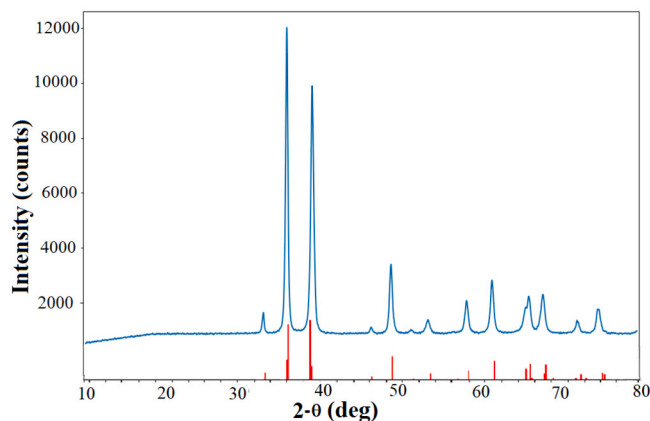
Fig. 2. XRD diffractogram of the copper oxide nanoparticles that were synthesized in this work. The inset shows the identification card of the corresponding structure as a reference.

(a)

(b)

(c)
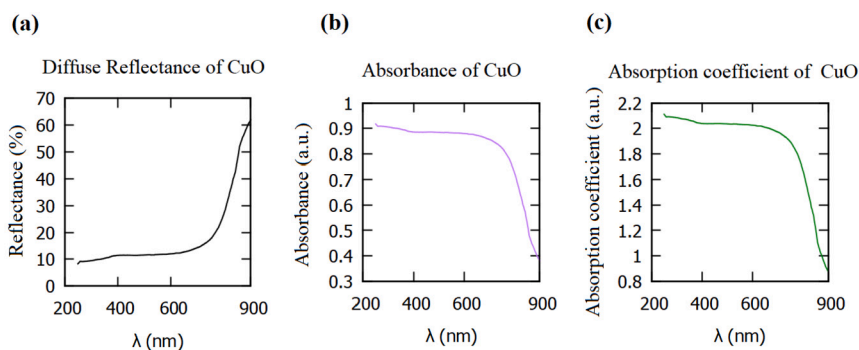
Fig. 3. Optical response profiles for the CuO (1 1 0) tenorite structure. (a) UV-Vis DRS, (b) Absorbance and (c) Absorption coefficient.

3. Results and discussion

3.1. Experimental section

3.1.1. X-Ray diffraction characterization

The XRD profile depicted in Fig. 2 clearly reveals the presence of the tenorite phase, since the characteristic peaks may be identified: 32.5° (110), 35.41° (11$\bar{1}$), 38.7° (111), 46.25° (11$\bar{2}$), 48.71° (20$\bar{2}$), 51.43° (112), 53.48° (020), 58.26° (202), 61.52 (11$\bar{3}$), 65.81 (022), 66.22 (31$\bar{1}$), 68.12 (220), 72.37 (311), 75.24 (22$\bar{2}$). This configuration corresponds to a monoclinic structure with lattice parameters a = 4.67 Å, b = 3.43 Å, c = 5.12 Å, and angles $\alpha = \gamma = 90°$, $\beta = 99.54°$, which are indexed with the PDF card 48-1548. Additionally, the crystal size was also calculated with the aid of the Scherrer relationship, as given by Eq. (2):

$$t = \frac{K\lambda}{\beta Cos(\theta)} \qquad (2)$$

where λ is the X-ray wavelength (given in Å), θ is the diffraction angle, t is the crystal size, K corresponds to the form factor of the crystal, and β is the full width at half maximum of the peak with largest intensity. The final size amounted to 24.51 nm.

Fig. 2 exhibits the XRD characterization of the copper oxide nanoparticles under study. The evaluation was performed in a 2θ interval ranging from 5° to 80°. The profile clearly suggests the presence of the tenorite phase, since the identification of such crystalline phase was performed by comparison with the JCPDS file No. 48-1548 for copper oxide, corresponding to tenorite. It gently fits the maxima shown in the experimental diffractogram.

3.1.2. Optical gap characterization

The results of the optical gap characterization are shown in Fig. 3 (a - c) in the visible range (200 - 900 nm). From the DRS measurements, it is possible to find the optical gap by applying Eq. (5), which considers the absorbance related directly with the path length of the incident light quantum crossing the sample, and also the intrinsic material properties. The relation used to describe such properties corresponds to the Kubelka-Munk equation, as given by:

$$F(R_\infty) = \frac{K}{S} = \frac{(1 - R_\infty)^2}{2R_\infty} \qquad (3)$$
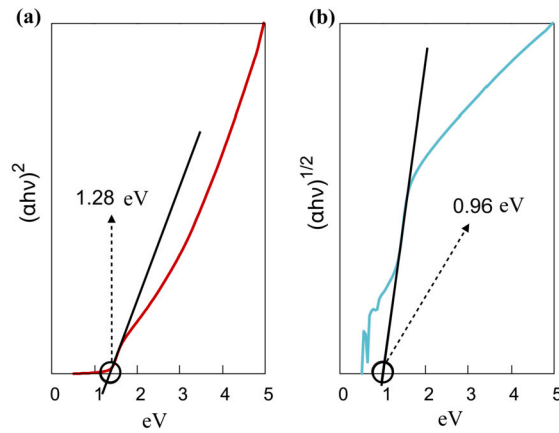
Fig. 4. Optical response profiles for the CuO (1 1 0) Tenorite, as obtained from Tauc's law. Absorption spectrum evidencing the presence of (a) Direct optical gap and (b) Absorption spectrum evidencing the presence of an indirect optical gap.
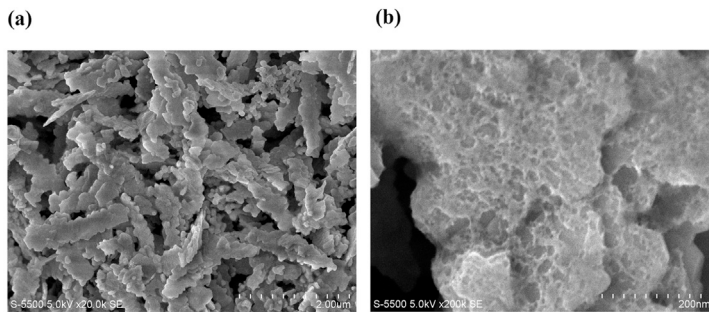
Fig. 5. SEM images of CuO. (a) 20 k× (um scale) and (b) 200 k× (nm scale).

in which R_∞ is the diffuse reflectance. Moreover, $R_\infty = \dfrac{R_{sample}}{R_{standar}}$. The parameters K and S are the absorption and dispersion coefficients in the material.

The term $K/S = (\alpha)$ depends on the energy in accordance to the following equation:

$$(\alpha h\nu)^n = A(h\nu - E_g) \tag{4}$$

Replacing the term α by the Eq. (3) in Eq. (4), it can then be further rewritten in the following form:

$$[F(R_\infty)h\nu]^n = A(h\nu - E_g) \tag{5}$$

In Eq. (5), h corresponds to the Planck constant, ν is the frequency of the incident light, A is a constant associated with the absorption intensity, and E_g is the band gap energy. The constant n represents values of 2 or 1/2, depending on the electronic gap nature of the material, which corresponds to a direct or indirect band gap, respectively. Fig. 4 (a, b) exhibits the results found from Eq. (5). That is, direct [Fig. 4(a)] and indirect [Fig. 4(b)]band gaps of 1.28 and 0.96 eV were experimentally evaluated, respectively.

The absorption coefficient is proportional to the absorbance by a factor known as the molar absorption factor. That is, to obtain the absorption coefficient, the absorbance was multiplied by the corresponding molar absorption factor, which can be obtained from the well-known Lambert-Beer law.

3.1.3. SEM characterization

The scanning electron microscopy images were acquired using a HITACHI equipment model S-550. In Fig. 5, the SEM images of copper oxide (CuO) are presented. In Fig. 5 (a), with a magnification of 20 k× (2 μm scale), a laminar shape with irregular edges and an approximate size of 2 μm can be observed. In Fig. 5 (b), the same material is shown, with a magnification of 200,000 k× (200 nm scale), which reveals an irregular surface with some edges and hollows.

3.2. Work function measurement

Ten measurements with the Kelvin probe were performed in accordance with the experimental methodology given in section 2.1. An average value of 5.13 eV was found, which is in close agreement with that obtained at the DFT level of 4.81 eV (as presented
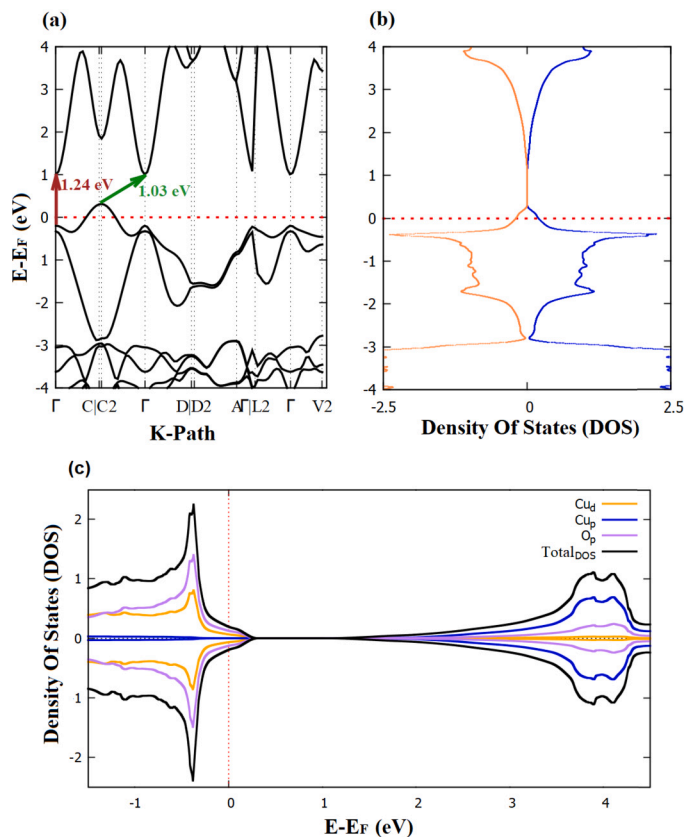
Fig. 6. (a) Electronic band structure of the CuO (1 1 0) tenorite. The doted red line represents the Fermi level. The brown and green arrows exhibit the direct and indirect band gaps, respectively. (b) Corresponding density of states (DOS) and (c) Projected density of states (PDOS).

below). That is, a difference of 6% with respect to the experimental value was observed. This gives to the theoretical model the adequate validity to be used in the subsequent calculations of this work.

3.3. Theoretical calculations

3.3.1. Electronic structure properties

The electronic structure properties were analyzed to assess the behavior of the tenorite. The band structure and density of states (DOS) of CuO (1 1 0) are depicted for the tenorite in Figs. 6 (a) and (b), respectively. In particular, the band structure exhibits two band gaps; namely, a direct band gap of 1.24 eV at the Γ point and an indirect gap of 1.03 eV from $Y2$ to the Γ point. Furthermore, as shown in Fig. 6(b), the DOS exhibits the antiferromagnetic state of CuO. Moreover, Fig. 6 (c) shows the band gap of CuO. The valence states are evidenced by hybridization of the O_{2p} (purple) and Cu_{3d} (orange) orbitals. However, the O_{2p} orbitals are predominant in valence states. The conduction band states are dominated by a small density of states corresponding to the Cu_{3p} (blue) orbitals. DOS and PDOS (projected density of states) [Fig. 6 (b) y (c)] shows the antiferromagnetic state of tenorite [40].

3.3.2. Work function and redox potential

The CuO (1 1 0) tenorite structure was subjected to a theoretical analysis to explore its photocatalytic potential to transform CO_2 into carbon compounds, capable of being used as solar fuel. The simulated work function (Φ) was calculated using the dipole correction in the geometric arrangement depicted in Fig. 7. An electric field was biased in the z-direction of the unit cell (see Fig. 7) to assess its effect caused by the interaction with the structure. The OV_∞ represents the electrostatic potential at the vacuum in the direction of the O-termination structure, while CuV_∞ represents the vacuum potential on the Cu-termination side. Φ was assessed with the aid of Eq. S3, as given in the Computational details section of the **SI**. That is, Φ was calculated on the Cu-termination side to explore its possible potential to allow the CO_2 molecule to evolve.

The vacuum potential on the Cu termination (CuV_∞) side corresponds to 6.33 eV, while the vacuum potential on the O termination (OV_∞) side is 8.36 eV. The energy at the Fermi level (E_F) is 1.52 eV. Therefore, the work function (Φ) (as computed from Eq. S3) for the CuO (1 1 0) surface (with Cu-termination) is 4.81 eV. This value is in close agreement with the experimental averaged result that amounts to 5.13 eV for CuO sample, as shown in Table S1 of SI.

That is, a difference of 6% with respect to the experimental value is observed. In this regard, we consider that the addition of more layers in the theoretical model would not increase the theoretical work function value, since the effect of the simulated
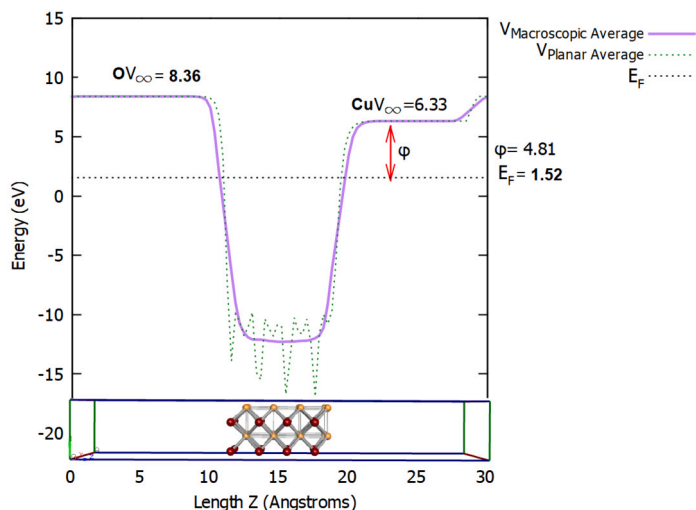
Fig. 7. Simulated potential with dipole-correction at the z direction to calculate the work function ϕ (marked with red arrows) of the tenorite (1 1 0) surface (at the bottom of the graph the unit cell used to the calculation is shown). OV_∞ and CuV_∞ correspond to the vacuum potential at the O- and Cu-termination faces respectively. E_F is the energy at the Fermi level.
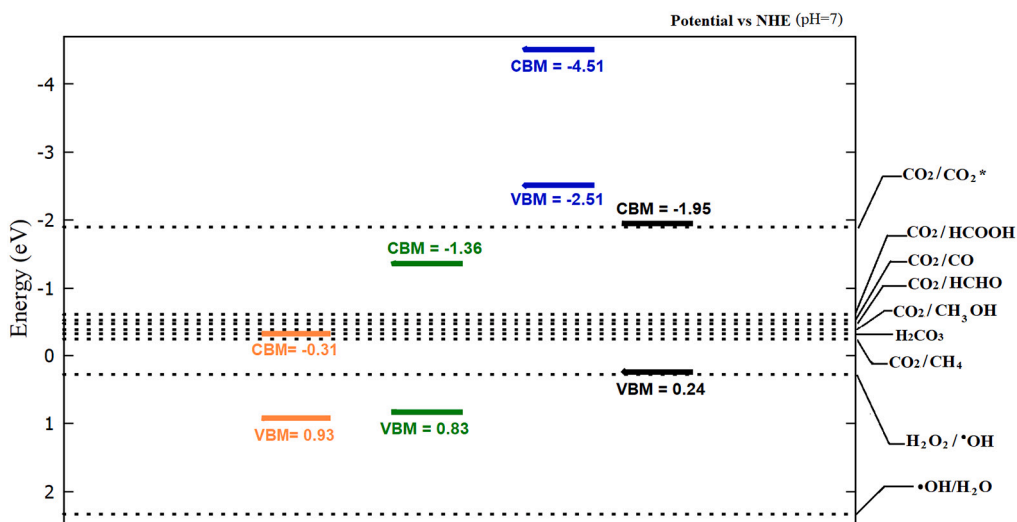
Fig. 8. Redox potential of the molecules of interest and the potential photocatalytic of the tenorite (1 1 0) (orange), the cuprite (1 0 0) (green), the cuprite (1 1 0) (blue) and the cuprite (1 1 1) (black).

electric field used for the calculations mainly interacts with the first layers of the model and the effect coming from deeper layers may be considered to be negligible. Based on the latter arguments and considering that the high performance computing (HPC) cost of the calculations rapidly increases for the string calculations (reaction routes) with the addition of more layers, we present our calculations with the 8 layers.

The conduction band minimum (CBM) and the valence band maximum (VBM) were evaluated in accordance to the Eq. S3 and S4, as given in the Computational Details section of the SI. Such parameters are intended to locate the energy levels at which the redox potential related to a given reaction is possible to reside. That is, those potentials inside that energy difference are more likely to evolve. The orange steps in Fig. 8 represent the CBM and VBM values for the CuO(1 1 0) tenorite structure; while the green, blue and black steps represent the same parameters of the Cu$_2$O (1 0 0), (1 1 0) and (1 1 1) for the sake of comparison (see Fig. 8). The cuprous oxide structure exhibits similar energy levels, which slightly changes the CBM and VBM values that allow them to support several CO$_2$ transformations. The structure of the CuO (1 1 0) tenorite shows a more selective catalytic potential that is primarily focused on the transformation from CO$_2$ to methane. Furthermore, the potential to transform CO$_2$ into methanol is marginally observed. As a consequence, tenorite acting as a catalyst may be implemented as a material to exclusively transform CO$_2$ to methane and methanol, both representing widely used solar fuels. As an additional remark, this selectivity could be advantageous since the pathway to fulfill the reaction could be performed in a smaller number of steps.
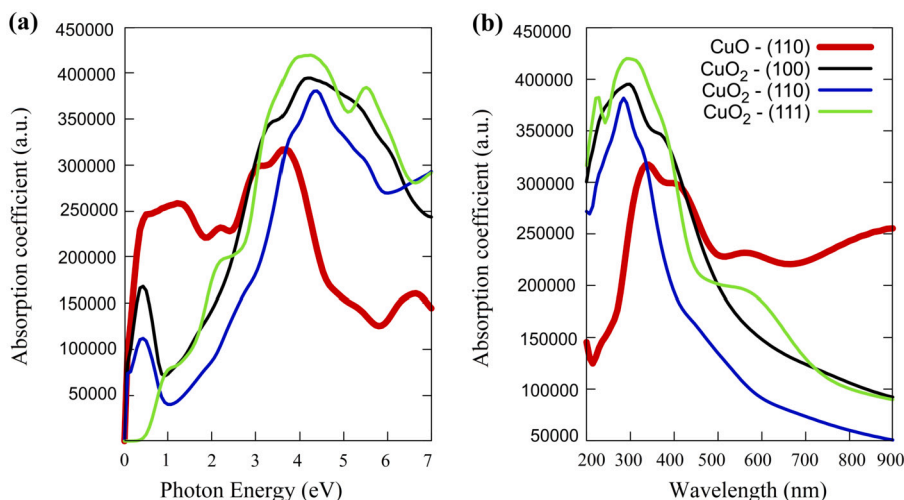
Fig. 9. Comparison of adsorption spectra for cuprous oxide and copper oxide nanostructures: (a) Photon Energy units, and (b) Wavelength units.

3.3.3. Theoretical optical properties

As it was previously described in the Computational details section, time-dependent density functional theory (TDDFT) computations were performed to simulate the absorption spectrum of $CuO(1\,1\,0)$ in order to elucidate the availability of the material to absorb solar light irradiation. The results are exhibited in Fig. 9, in which the absorption coefficient profiles are plotted with respect to the photon energy (see Fig. 9 (a)), and with respect to the wavelength (as depicted in Fig. 9 (b)). A maximum is located near the ultraviolet region for the $CuO\,(1\,1\,0)$ system. A second maximum is identified at approximately 400 nm, which could be addressed to an enhanced potential to absorb visible light coming from solar light irradiation. Moreover, the spectrum extends all over the range of visible light, with an increasing behavior in the infrared region. For the sake of comparison, the absorption spectra of analogous copper systems were also calculated. The spectra of the metal oxide surfaces $CuO_2\,(1\,0\,0)$, $(1\,1\,0)$ and $(1\,1\,1)$ and $CuO\,(1\,1\,0)$ are shown in Fig. 9 (a) and (b). Such spectra reveal their maxima located at the ultraviolet region, and a long tail extending throughout all the visible light range. As depicted in Fig. 9 (b), the long tails of the CuO_2 surfaces remain under the contribution coming from the $CuO\,(1\,1\,0)$ system. This could be interpreted as an improved potential that intrinsically increases in the $CuO\,(1\,1\,0)$ system. That is, the tenorite is expected to capture a larger amount of visible light than the cuprite structure at different facets. This behavior testifies to the increased availability of tenorite to allow a photocatalytic reaction to proceed with respect to that observed in the typical cuprite structure [41].

Additionally, the diffuse reflectance measurements previously presented in section 3.1.2, also corroborate the theoretical observations. That is, Fig. 3 exhibits the absorption coefficient of the tenorite structure in the range of 200 nm to 900 nm. It is important to note that the behavior of the absorption coefficient is kept constant in the visible range, which is in close agreement with the theoretical results given above. It addresses the enhanced availability that CuO tenorite shows to absorb solar light irradiation. This may be applied directly for a photocatalytic procedure. Such results are also in agreement with previous observations [41]. The performance of the tenorite with respect to cuprite (CuO_2) could be inferred from the nature of direct and indirect band gaps; as it was evidenced from both approaches, namely theoretical and experimental. That is, such electronic structure disposition gives the tenorite more accessible states to absorb visible light irradiation and, as a consequence, improves its potential to be adopted as a photocatalytic material.

3.3.4. Photocatalytic CO_2 transformation

DFT calculations performed at the PBE + ZORA approach revealed the different reaction mechanisms involved in the evolution reaction of the CO_2 transformation. The transformation begins with CO_2 activation through the $^{\bullet}OH$ radical attack. This radical is formed by the H_2O_2 reduction as previously observed [17]. The final step considered in this simulation is the formation of orthocarbonic acid ($C(OH)_4$), due to the attack of another $^{\bullet}OH$ radical on the carbonic acid. Although $C(OH)_4$ is considered highly unstable, its formation on the tenorite surface is feasible, as has been shown in this work. This is likely due to the narrow potential of the tenorite, which requires an energy barrier to dissociate this molecule into more stable species.

The following reaction pathways are proposed for the CO_2 evolution reaction onto the $CuO\,(1\,1\,0)$ surface in the presence of a light source. This process is simulated by considering that the electron-hole formation was originally induced:

$$CO_2 + H_2O_2 + e^- \longrightarrow CO_2 + {^{\bullet}OH} + [OH]^- \tag{6}$$

$$CO_2 + {^{\bullet}OH} + e^- \longrightarrow [HCO_3]^- \tag{7}$$

$$[HCO_3]^- + [H]^+ \longrightarrow H_2CO_3 \tag{8}$$

$$H_2CO_3 + H_2O_2 + e^- \longrightarrow H_2CO_3 + {^{\bullet}OH} + [OH]^- \tag{9}$$
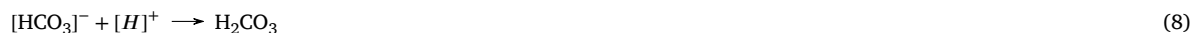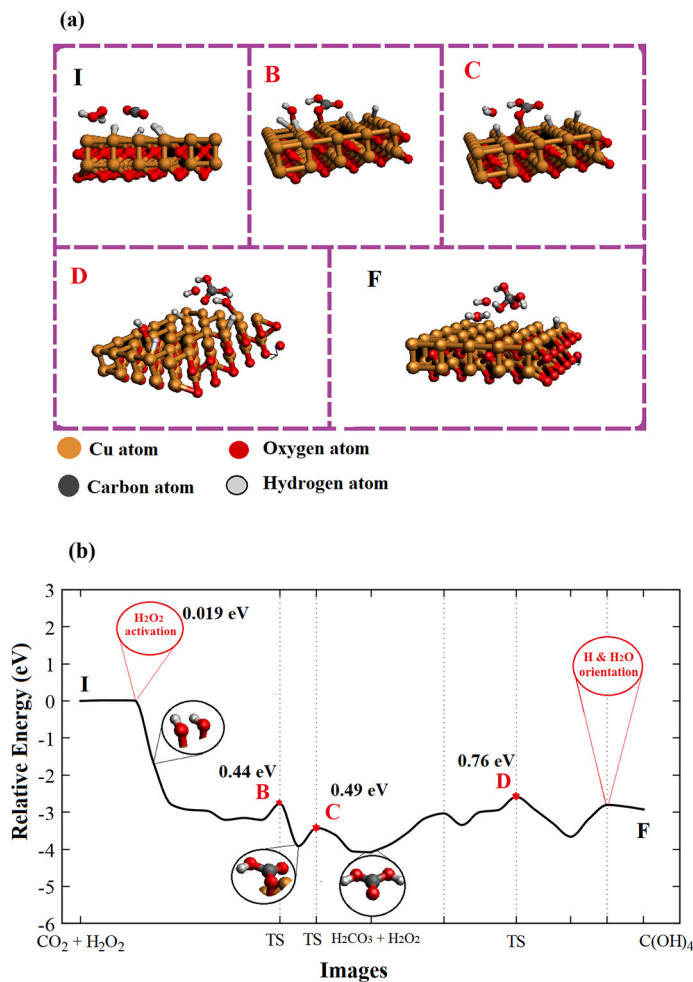
Fig. 10. (a) Geometries of the most relevant steps in the reaction path: *I* and *F* are initial and final geometries, respectively. *B*, *C* and *D* are the three transition states that were identified for the reaction path. (b) Relative energy profile for the evolution of the reaction path, as proposed in Eq. (6) - (10). The TS's are labeled in red and the corresponding energy barriers are also given. In item (b), the rise of the species; namely, $^\bullet OH$, $[HCO_3]^-$ and H_2CO_3 is also depicted.

$$H_2CO_3 + {}^\bullet OH + [H]^+ + e^- \longrightarrow C(OH)_4 \qquad\qquad (10)$$
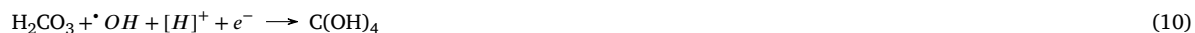
The reaction mechanisms proposed in Eq. (6) - (10) were studied at the DFT level by using the string method as given in the computational details. This methodology allows us to predict the most probable reaction pathway on the potential energy surface (PES).

At the first step, the H_2O_2 species adsorbed onto the CuO surface was reduced by an electron e^- removed from the catalyst, forming as a consequence an $^\bullet OH$ radical and the respective $[OH]^-$ anion, with virtually null activation energy (0.019 eV). The $^\bullet OH$ radical attacks the CO_2 molecule and, with the aid of an e^-, it forms the HCO_3^- bicarbonate anion. Such an anion, in the presence of the H^+ proton, is eventually transformed into carbonic acid H_2CO_3. In step 4, which is described by Eq. (9), another H_2O_2 unit is also reduced by an e^- and forms another $^\bullet OH/[OH]^-$ pair. This new $^\bullet OH$ radical attacks the H_2CO_3 double bond (C=O) and with a $[H]^+$ + e^-, the $C(OH)_4$ arises. It is important to highlight that $C(OH)_4$ is highly unstable as an isolated molecule. In this work, it is shown that this molecule is stabilized due to the interaction with the tenorite surface. The energy barrier of this reaction path corresponds to the TS *D*, shown in Fig. 10 (b). It amounts to 0.79 eV and corresponds to the H_2CO_3 activation, as it can be seen in Fig. 10 (a). The TS, *B* and *C* correspond to H diffusion for water formation and $[HCO_3]^-$ hydrogenation, respectively. The adsorption energies for the molecules of interest were computed in accordance with Eq. (1) of the Computational Details section, and such results are listed in Table 1.

It is important to denote that the DFT methodology was applied to search the lowest-energy configuration, it guarantees that a stable attraction was found. Additionally, the adsorption energy of the $C(OH)_4$ onto the tenorite surface amounts to -2.11 eV, which can be addressed to a chemisorption interaction type. Additionally, a frequency calculation analysis was performed for the $C(OH)_4$ system. The frequencies are presented in Table S7 of **SI**, exhibiting that all values are real, with no imaginary frequencies. This indicates that the lowest energy configuration previously found represents a minimum in the potential energy surface, and also guarantees that a stable molecular geometry was obtained.

Table 1
Adsorption energies of the species of interest along the transformation steps of CO_2 onto the CuO (1 1 0) surface.

Species	Adsorption energy (eV)
CO_2	-0.89
H_2O_2	-1.27
H_2CO_3	-1.46
$C(OH)_4$	-2.11

Fig. S1 of SI depicts the electronic density difference at the interface of the organic species, and the tenorite structure at the respective transition state (TS). The two-dimensional slice shows a large contribution at the periphery of the intermediate structures, revealing that an effective electronic transfer is triggered at this step. Consequently, such charge excess is used by the organic species to promote the formation of the $C(OH)_4$ at the products state (as it is shown in Fig. S1 of SI). Such a behavior is corroborated by the Bader charge calculations, revealing an electronic excess at the oxygen atoms at the transition state of the reaction. This is presented from Table S2 to Table S7 of SI.

In Table 1, the adsorption energies are listed. The highest adsorption energy is presented by the $C(OH)_4$ molecule with -2.11 eV. This result and the charge density isosurfaces presented in **SI**, suggest a strong interaction between this molecule and the tenorite (1 1 0) surface. Moreover, the rest of the molecules involved in the reaction path, also present an interaction with the surface, which is a requirement for a photocatalysis process to be feasible. Particularly, the H_2O_2 molecule shows a higher adsorption energy (-1.27 eV) than the CO_2 (-0.89 eV). This contributes to the H_2O_2 molecule to form the ${}^{\bullet}OH$ radical onto the CuO(1 1 0) surface.

As a final remark, it is worth mentioning that the feasibility of the CO_2 transformation into the carbon compounds may be assessed from the activation energies obtained theoretically via the string methodology. In this respect, we performed a comparison with respect to other metal oxide catalysts previously studied somewhere else [17,42–45]. In particular, some analogous catalysts are presented in Table S8 of SI. The activation energies in the transformation of CO_2, are even doubled those values observed for the tenorite structure. This behavior addresses a large potential to the tenorite system to be implemented in photocatalytic applications.

4. Conclusions

Theoretical calculations and experimental measurements evidenced the photocatalytic potential of tenorite, which is limited to some feasible reaction routes, including the CO_2 evolution reaction. That is, the material is selective toward certain products, such as methanol and methane. It was theoretically exhibited that the ${}^{\bullet}OH$ radical formation is virtually immediate, since it is shown that in the first step, the energy barrier amounts to 0.019 eV. This is of interest for studies where free radical attack reactions are involved. Furthermore, a transformation of CO_2 can be initiated by an addition reaction of the ${}^{\bullet}OH$ radical to obtain carbonic acid. Additionally, it was theoretically shown that carbonic acid can also react with other ${}^{\bullet}OH$ radical to form orthocarbonic acid, an unstable compound that appears to stabilize on the surface of tenorite, according to theoretical calculations. That is, the species is formed with sufficient stability to maintain its structure and be adsorbed on the surface. However, its reaction energy is higher than that of the previous energy step, where carbonic acid is formed. Therefore, as expected, orthocarbonic acid is less stable than carbonic acid, and the last step of the reaction would correspond to an endergonic reaction. The direct and indirect band gaps observed with UV-vis DRS experiments and also with electronic band calculations may influence the availability of tenorite to absorb solar light irradiation, giving the material an enhanced potential for photocatalytic applications with respect to other copper oxides.

The experimental evidence via SEM images revealed an adequate morphology to perform catalytic activity. Moreover, the experimental measurement of the work function with the Kelvin probe exhibited an averaged value of 5.13 eV that differs by 6% with respect to that obtained theoretically. The band gap value is also in close agreement with the theoretical calculations. Such evidence gives the DFT modeling the availability to predict novel processes on the tenorite, such as the CO_2 transformations described in the present work.

CRediT authorship contribution statement

O. Castro-Ocampo, Christian A. Celaya, Jesús Muñiz: Analyzed and interpreted the data; Wrote the paper.
J. C. Ochoa-Jaimes: Conceived and designed the experiments; Performed the experiments.
J. González-Torres Analyzed and interpreted the data.
L. González-Reyes: Conceived and designed the experiments.
I. Hernández-Pérez: Conceived and designed the experiments; Analyzed and interpreted the data.
V. Garibay-Febles: Conceived and designed the experiments.
Oscar A. Jaramillo-Quintero, R. Suárez-Parra: Conceived and designed the experiments; Contributed reagents, materials, analysis tools or data.

Declaration of competing interest

The authors declare that they have no known competing financial interests or personal relationships that could have appeared to influence the work reported in this paper.

Data availability

Data included in article/supp. material/referenced in article.

Acknowledgements

Appendix A. Supplementary material

Supplementary material related to this article can be found online at https://doi.org/10.1016/j.heliyon.2023.e20134.

References

[1] H. Paeth, A. Scholten, P. Friederichs, A. Hense, Uncertainties in climate change prediction: El Niño-Southern Oscillation and monsoons, Glob. Planet. Change 60 (3) (2008) 265–288, https://doi.org/10.1016/j.gloplacha.2007.03.002.

[2] D.J. Hofmann, J.H. Butler, P.P. Tans, A new look at atmospheric carbon dioxide, Atmos. Environ. 43 (12) (2009) 2084–2086, https://doi.org/10.1016/j.atmosenv.2008.12.028.

[3] K. Li, B. Peng, T. Peng, Recent advances in heterogeneous photocatalytic CO_2 conversion to solar fuels, ACS Catal. 6 (11) (2016) 7485–7527, https://doi.org/10.1021/acscatal.6b02089.

[4] J. He, C. Janáky, Recent advances in solar-driven carbon dioxide conversion: expectations versus reality, ACS Energy Lett. 5 (6) (2020) 1996–2014, https://doi.org/10.1021/acsenergylett.0c00645.

[5] W. Tu, Y. Zhou, Z. Zou, Photocatalytic conversion of CO_2 into renewable hydrocarbon fuels: state-of-the-art accomplishment, challenges, and prospects, Adv. Mater. 26 (27) (2014) 4607–4626, https://doi.org/10.1002/adma.201400087.

[6] K. Li, X. An, K.H. Park, M. Khraisheh, J. Tang, A critical review of CO_2 photoconversion: catalysts and reactors, Catal. Today 224 (2014) 3–12, https://doi.org/10.1016/j.cattod.2013.12.006.

[7] G. Zhao, X. Huang, X. Wang, X. Wang, Progress in catalyst exploration for heterogeneous CO_2 reduction and utilization: a critical review, J. Mater. Chem. A 5 (2017) 21625–21649, https://doi.org/10.1039/C7TA07290D.

[8] S. Hussain, Y. Wang, L. Guo, T. He, Theoretical insights into the mechanism of photocatalytic reduction of CO_2 over semiconductor catalysts, J. Photochem. Photobiol., C, Photochem. Rev. 52 (2022) 100538, https://doi.org/10.1016/j.jphotochemrev.2022.100538.

[9] W. Fan, Q. Zhang, Y. Wang, Semiconductor-based nanocomposites for photocatalytic H_2 production and CO_2 conversion, Phys. Chem. Chem. Phys. 15 (2013) 2632–2649, https://doi.org/10.1039/C2CP43524A.

[10] T.-F. Yeh, J. Cihlář, C.-Y. Chang, C. Cheng, H. Teng, Roles of graphene oxide in photocatalytic water splitting, Mater. Today 16 (3) (2013) 78–84, https://doi.org/10.1016/j.mattod.2013.03.006.

[11] Y. Wang, Y. Tian, L. Yan, Z. Su, DFT study on sulfur-doped g-C_3N_4 nanosheets as a photocatalyst for CO_2 reduction reaction, J. Phys. Chem. C 122 (14) (2018) 7712–7719, https://doi.org/10.1021/acs.jpcc.8b00098.

[12] M. Méndez-Galván, C.A. Celaya, O.A. Jaramillo-Quintero, J. Muñiz, G. Díaz, H.A. Lara-García, Tuning the band gap of M-doped titanate nanotubes (M = Fe, Co, Ni, and Cu): an experimental and theoretical study, Nanoscale Adv. 3 (2021) 1382–1391, https://doi.org/10.1039/D0NA00932F.

[13] S. Guo, S. Zhang, Y. Guo, J.C. Yu, Graphene oxide–Fe_2O_3 hybrid material as highly efficient heterogeneous catalyst for degradation of organic contaminants, Carbon 60 (2013) 437–444, https://doi.org/10.1016/j.carbon.2013.04.058.

[14] D.-H. Lim, J.H. Jo, D.Y. Shin, J. Wilcox, H.C. Ham, S.W. Nam, Carbon dioxide conversion into hydrocarbon fuels on defective graphene-supported Cu nanoparticles from first principles, Nanoscale 6 (2014) 5087–5092, https://doi.org/10.1039/C3NR06539A.

[15] P. Mishra, P. Saravanan, G. Packirisamy, M. Jang, C. Wang, A subtle review on the challenges of photocatalytic fuel cell for sustainable power production, Int. J. Hydrog. Energy 46 (44) (2021) 22877–22906, https://doi.org/10.1016/j.ijhydene.2021.04.109.

[16] Daniel G. Araiza, Christian A. Celaya, Antonio Gómez-Cortés, Samuel Tehuacanero-Cuapa, J. Noé Díaz de León, Jesús Muñiz, Hugo Lara-García, Gabriela Díaz, Cobalt-ceria catalysts for the methanol decomposition: insights in the long-term stability and methanol interaction, Top. Catal. 65 (2022) 1331–1346, https://doi.org/10.1007/s11244-022-01667-6.

[17] O. Castro-Ocampo, Christian A. Celaya, L. González-Reyes, I. Hernández-Pérez, V. Garibay-Febles, Oscar A. Jaramillo-Quintero, Hugo A. Lara-García, Jesús Muñiz, R. Suárez-Parra, Understanding hydroxyl radicals addition to CO_2 on α-Fe_2O_3(1 1 0) surface photocatalyst for organic compounds production, Fuel 310 (2022) 122465, https://doi.org/10.1016/j.fuel.2021.122465.

[18] K. Wang, Y. Liu, Q. Wang, Y. Zhang, X. Yang, L. Chen, M. Liu, X. Qiu, J. Li, W. Li, Asymmetric Cu-N sites on copper oxide photocathode for photoelectrochemical CO_2 reduction towards C_2 products, Appl. Catal. B 316 (2022) 121616, https://doi.org/10.1016/j.apcatb.2022.121616.

[19] W. Guo, S. Liu, X. Tan, R. Wu, X. Yan, C. Chen, Q. Zhu, L. Zheng, J. Ma, J. Zhang, Y. Huang, X. Sun, B. Han, Highly efficient CO_2 electroreduction to methanol through atomically dispersed Sn coupled with defective CuO catalysts, Angew. Chem., Int. Ed. 60 (40) (2021) 21979–21987, https://doi.org/10.1002/anie.202108635.

[20] T. Jia, L. Wang, L. Zhang, Z. Zhu, K. Zhang, B. Zhu, X. Li, C. Zhai, S. Li, Y. Zhou, H. Tao, Engineering vacancy and hydrophobicity of spherical coral-like CuO catalyst for effective electrochemical CO_2 reduction to ethylene, Surf. Interfaces 38 (2023) 102841, https://doi.org/10.1016/j.surfin.2023.102841.

[21] J.L.V. Moreno, A.A.B. Padama, H. Kasai, A density functional theory-based study on the dissociation of NO on a CuO(110) surface, CrystEngComm 16 (2014) 2260–2265, https://doi.org/10.1039/C3CE42103A.

[22] X.X. Jiang, X. De Hu, M. Tarek, P. Saravanan, R. Alqadhi, S.Y. Chin, M.M. Rahman Khan, Tailoring the properties of g-C_3N_4 with CuO for enhanced photoelectrocatalytic CO_2 reduction to methanol, J. CO2 Util. 40 (2020) 101222, https://doi.org/10.1016/j.jcou.2020.101222.

[23] R. Michal, E. Dworniczek, M. Caplovicova, O. Monfort, P. Lianos, L. Caplovic, G. Plesch, Photocatalytic properties and selective antimicrobial activity of TiO_2(Eu)/CuO nanocomposite, Appl. Surf. Sci. 371 (2016) 538–546, https://doi.org/10.1016/j.apsusc.2016.03.003.

[24] M. Haddad, A. Belhadi, L. Boudjellal, M. Trari, Photocatalytic hydrogen production on the hetero-junction CuO/ZnO, in: International Symposium on Sustainable Hydrogen 2019, Int. J. Hydrog. Energy 46 (75) (2021) 37556–37563, https://doi.org/10.1016/j.ijhydene.2020.11.053.

[25] R.G. Parr, Y. Weitao, Density-Functional Theory of Atoms and Molecules, International Series of Monographs on Chemistry, Oxford University Press, USA, 1994.

[26] P. Giannozzi, O. Andreussi, T. Brumme, O. Bunau, M.B. Nardelli, M. Calandra, R. Car, C. Cavazzoni, D. Ceresoli, M. Cococcioni, N. Colonna, I. Carnimeo, A.D. Corso, S. de Gironcoli, P. Delugas, R.A.D. Jr, A. Ferretti, A. Floris, G. Fratesi, G. Fugallo, R. Gebauer, U. Gerstmann, F. Giustino, T. Gorni, J. Jia, M. Kawamura, H.-Y. Ko, A. Kokalj, E. Küçükbenli, M. Lazzeri, M. Marsili, N. Marzari, F. Mauri, N.L. Nguyen, H.-V. Nguyen, A.O. de-la Roza, L. Paulatto, S. Poncé, D. Rocca, R. Sabatini, B. Santra, M. Schlipf, A.P. Seitsonen, A. Smogunov, I. Timrov, T. Thonhauser, P. Umari, N. Vast, X. Wu, S. Baroni, Advanced capabilities for materials modelling with QUANTUM ESPRESSO, J. Phys. Condens. Matter 29 (46) (2017) 465901.

[27] J.P. Perdew, K. Burke, M. Ernzerhof, Generalized gradient approximation made simple, Phys. Rev. Lett. 77 (1996) 3865–3868, https://doi.org/10.1103/PhysRevLett.78.1396.

[28] X. Huang, S.K. Ramadugu, S.E. Mason, Surface-specific $DFT + U$ approach applied to α-Fe_2O_3(0001), J. Phys. Chem. C 120 (9) (2016) 4919–4930, https://doi.org/10.1021/acs.jpcc.5b12144.

[29] B. Himmetoglu, R.M. Wentzcovitch, M. Cococcioni, First-principles study of electronic and structural properties of CuO, Phys. Rev. B 84 (2011) 115108, https://doi.org/10.1103/PhysRevB.84.115108.

[30] H.J. Monkhorst, J.D. Pack, Special points for Brillouin-zone integrations, Phys. Rev. B 13 (1976) 5188–5192, https://doi.org/10.1103/PhysRevB.13.5188.

[31] W. E, W. Ren, E. Vanden-Eijnden, String method for the study of rare events, Phys. Rev. B 66 (2002) 052301, https://doi.org/10.1103/PhysRevB.66.052301.

[32] W. E, W. Ren, E. Vanden-Eijnden, Simplified and improved string method for computing the minimum energy paths in barrier-crossing events, J. Chem. Phys. 126 (16) (2007), https://doi.org/10.1063/1.2720838.

[33] V. Blum, R. Gehrke, F. Hanke, P. Havu, V. Havu, X. Ren, K. Reuter, M. Scheffler, Ab initio molecular simulations with numeric atom-centered orbitals, Comput. Phys. Commun. 180 (11) (2009) 2175–2196, https://doi.org/10.1016/j.cpc.2009.06.022.

[34] V. Havu, V. Blum, P. Havu, M. Scheffler, Efficient $O(N)$ integration for all-electron electronic structure calculation using numeric basis functions, J. Comput. Phys. 228 (22) (2009) 8367–8379, https://doi.org/10.1016/j.jcp.2009.08.008.

[35] X. Ren, P. Rinke, V. Blum, J. Wieferink, A. Tkatchenko, A. Sanfilippo, K. Reuter, M. Scheffler, Resolution-of-identity approach to Hartree–Fock, hybrid density functionals, RPA, MP2 and GW with numeric atom-centered orbital basis functions, New J. Phys. 14 (5) (2012) 053020, https://doi.org/10.1088/1367-2630/14/5/053020.

[36] A. Tkatchenko, M. Scheffler, Accurate molecular van der Waals interactions from ground-state electron density and free-atom reference data, Phys. Rev. Lett. 102 (2009) 073005, https://doi.org/10.1103/PhysRevLett.102.073005.

[37] E. van Lenthe, J.G. Snijders, E.J. Baerends, The zero-order regular approximation for relativistic effects: the effect of spin–orbit coupling in closed shell molecules, J. Chem. Phys. 105 (15) (1996) 6505–6516, https://doi.org/10.1063/1.472460.

[38] G. Henkelman, B.P. Uberuaga, H. Jónsson, A climbing image nudged elastic band method for finding saddle points and minimum energy paths, J. Chem. Phys. 113 (22) (2000) 9901–9904, https://doi.org/10.1063/1.1329672.

[39] P. López-Caballero, A.W. Hauser, M. Pilar de Lara-Castells, Exploring the catalytic properties of unsupported and TiO_2-supported Cu_5 clusters: CO_2 decomposition to CO and CO_2 photoactivation, J. Phys. Chem. C 123 (37) (2019) 23064–23074, https://doi.org/10.1021/acs.jpcc.9b06620.

[40] H. Cao, Z. Zhou, J. Yu, X. Zhou, DFT study on structural, electronic, and optical properties of cubic and monoclinic CuO, J. Comput. Electron. 17 (1) (2018) 21–28, https://doi.org/10.1007/s10825-017-1057-9.

[41] H. Zhang, K. Wang, L. Wang, H. Xie, W. Yu, Mesoporous CuO with full spectrum absorption for photothermal conversion in direct absorption solar collectors, Sol. Energy 201 (2020) 628–637, https://doi.org/10.1016/j.solener.2020.03.047.

[42] T. Otroshchenko, G. Jiang, V.A. Kondratenko, U. Rodemerck, E.V. Kondratenko, Current status and perspectives in oxidative, non-oxidative and CO_2-mediated dehydrogenation of propane and isobutane over metal oxide catalysts, Chem. Soc. Rev. 50 (1) (2021) 473–527, https://doi.org/10.1039/D0CS01140A.

[43] C.A. Celaya, C. Delesma, S. Torres-Arellano, P. Sebastian, J. Muñiz, Understanding CO_2 conversion into hydrocarbons via a photoreductive process supported on the Cu_2O(100), (110) and (111) surface facets: a first principles study, Fuel 306 (2021) 121643, https://doi.org/10.1016/j.fuel.2021.121643.

[44] C.A. Celaya, M. Méndez-Galván, O. Castro-Ocampo, L.M. Torres-Martínez, E. Luévano-Hipólito, J.N. Díaz de León, H.A. Lara-García, G. Díaz, J. Muñiz, Exploring the CO_2 conversion into hydrocarbons via a photocatalytic process onto M-doped titanate nanotubes (M = Ni and Cu), Fuel 324 (2022) 124440, https://doi.org/10.1016/j.fuel.2022.124440.

[45] E. Tayyebi, J. Hussain, Y. Abghoui, E. Skúlason, Trends of electrochemical CO_2 reduction reaction on transition metal oxide catalysts, J. Phys. Chem. C 122 (18) (2018) 10078–10087, https://doi.org/10.1021/acs.jpcc.8b02224.